Wind Stress Curl Forcing of the Coastal Ocean near Point Conception, California*

ANDREAS MÜNCHOW

Institute of Marine and Coastal Sciences, Rutgers, The State University of New Jersey, New Brunswick, New Jersey

(Manuscript received 18 March 1999, in final form 8 July 1999)

ABSTRACT

Near Point Conception, California, the atmospheric flow separates from the coast and a large wind stress curl results. Direct spatial wind field observations from 20 aircraft overflights in the spring of 1983 suggest that Ekman pumping of on average 4 m day^{-1} contributes to the local dynamics. During strong and persistent upwelling events the curl-driven Ekman pumping reaches up to 20 m day^{-1}. A single complex empirical orthogonal function explains more than 72% of the spatial and temporal wind stress variance. It reveals large wind stress curl at the center of the western Santa Barbara Channel entrance. This dominant mode correlates strongly ($r^2 = 0.79$) with the wind stress observed at a moored buoy. The location of largest Ekman pumping in the ocean indicated by this mode coincides with the location of a laterally sheared, cyclonic flow. Cold upwelled waters enter the Santa Barbara Channel along its southern perimeter while warm, and thus buoyant, waters from the Southern California Bight exit the channel along its northern perimeter. Buoy wind stress and lateral current shear at 30-m depth correlate significantly at periods of about 3.5 and 6 days with phase lags of about 0.5 and 2 days, respectively. Hydrographic observations from 1983 do not, however, indicate effects of Ekman pumping on the internal mass field as winds vary in speed and direction at daily timescales. This contrasts with 1984 observations that do indicate strong doming of isopycnals over the center of the channel at its western entrance. Winds prior to and during hydrographic observations in the spring of 1984 were both stronger and more steady than they were in 1983. Cyclonic shears reach $0.4f$ at the entrance of the Santa Barbara Channel near Point Conception; here f is the planetary vorticity. The thermal wind balance explains the lateral shear of the alongchannel surface flow rather well.

1. Introduction

The study of wind-forced motions in the coastal ocean has a long history that probably began with Fridtjof Nansen who, during the 1893–1896 Norwegian expedition to drift with the ice across the Arctic Ocean, discovered peculiar ice motions to the right of the wind. He subsequently attributed this motion to the earth's rotation (Nansen 1902). His qualitative conjecture motivated Walfried Ekman to study this effect using the laws of motion that Bjerknes (1901) had just formulated for the ocean and atmosphere. A landmark paper resulted (Ekman 1905), that, I believe, marked the beginning of coastal physical oceanography. Three decades later, another Arctic explorer, Harald Sverdrup, was the first to quantify wind-forced upwelling along the California coast. Using an inferred vertical upwelling velocity from successive density observations along with mass conservation, Sverdrup (1938) presented the first velocity section across the California shelf and slope seas. He concluded that ''. . . the processes are far more complicated than assumed on the basis of earlier data.'' Ongoing and planned observational research on eastern boundary currents off California and elsewhere attests to this statement.

Just 50 km to the south of Sverdrup's 1937 sections, the California coastline changes its orientation at Point Conception by 90 degrees from north–south to east–west. Several large observational experiments took place near Point Conception during the last two decades. Early work focused either on Point Conception or on the Santa Barbara Channel while more recent work resolved the coupling between these two domains. Brink et al. (1984) described the local atmospheric velocity and the oceanic density fields during the spring 1981 transition. They found a complex three-dimensional density field that responded to the local upwelling-favorable winds. The study commented on the spatial variability of the wind field, but wind observations were insufficient to statistically analyze its spatial variability.

During the spring of 1983 several investigators collected data with ships and aircraft in an extensive study of the meteorology and oceanography near Point Con-

* Institute of Marine and Coastal Sciences Contribution Number 98-26.

Corresponding author address: Andreas Münchow, The Graduate College of Marine Studies, University of Delaware, Robinson Hall, Newark, DE 19716-3501.
E-mail: andreas@udel.edu

ception. Atkinson et al. (1986) outline the experiment and discuss the hydrographic variability. Brink and Muench (1986) and Auad et al. (1998) dynamically analyze velocity measurements from this and a subsequent 1984 experiment for coastally trapped oscillating motions at subtidal timescales. Münchow (1998) describes diurnal and semidiurnal tidal currents. Barth and Brink (1987) study oceanic dynamics with data from a vessel-mounted acoustic Doppler current profiler. Emphasizing data from one particular upwelling event, they conceptualize the oceanic flow near Point Conception as an upwelling center with a cold plume that extends more than 80 km offshore. More recently Strub et al. (1991) interpret such plumes near capes off California as meanders of the California Current system. Furthermore, the cold plume near Point Conception frequently enters the Santa Barbara Channel instead of moving offshore. Barth and Brink (1987) thus describe only one of many responses of the coastal ocean near Point Conception to the generally upwelling-favorable winds. Using more recent data, Harms and Winant (1998) and Dever et al. (1998) study low-frequency surface circulation in the Santa Barbara Channel with current meter mooring and drifter data, respectively. They find a complex circulation that they classify in terms of reoccurring synoptic patterns suggested by empirical orthogonal functions (EOFs). They both comment on the forcing by the local winds, associated upwelling, as well as barotropic and baroclinic pressure gradients.

Halliwell and Allen (1987) review the atmospheric circulation along the entire U.S. West Coast for the period of 1981–82 while Dorman and Winant (1995) statistically analyze wind signals for the period of 1981–90. Each winter passing cyclones and anticyclones cause coastal winds that vary with time. In contrast, during the spring and summer seasons an almost stationary high pressure system over the subtropical Pacific and a low pressure system over the southwestern deserts of the United States cause strong and persistent southward winds along the coasts of California. The transition from the winter to the spring/summer regime generally occurs within a few days in March or April (Strub et al. 1987). The largest wind velocities occur at the height of a temperature inversion that caps the cool and moist air of a well-mixed marine layer from hot and dry air of the upper atmosphere (Beardsley et al. 1987). The thickness of the marine layer decreases from about 2000 m near Hawaii to less than 200 m off California and appears to be in thermal wind balance (Beardsley et al. 1987). Northward propagating ageostrophic events such as Kelvin waves and nonlinear gravity currents, however, occasionally disrupt the steady southward flow (Dorman 1987; Hermann et al. 1990; Mass and Albright 1987).

Topographic features such as capes and headlands perturb and sometimes accelerate the flow to the point where it becomes supercritical (Winant et al. 1988). No perturbations can then propagate upstream and their kinetic energy is often trapped near such regions. The wind field along the coast near Point Conception has been analyzed by Caldwell et al. (1986) with time series data. They emphasize temporal variability, but nevertheless find a wind field that varies along the coast. Their data, however, are inadequate to study the effect of the local wind stress curl since most of their wind stations are on land. The data thus do not resolve the wind field over the ocean where most of the spatial variability occurs. In a different study, Eddington et al. (1992) model the winds near Point Conception with a layer model that features an active lower marine layer and a stagnant atmosphere above. Their process study successfully reproduces both a wind maximum south of Point Conception and the large horizontal wind shears across the western entrance of the Santa Barbara Channel. Similar observational and theoretical studies are reported for the CODE region off Northern California by Enriquez and Friehe (1995) and Samelson (1992).

Here I investigate the spatially variable wind field at the western entrance of the Santa Barbara Channel near Point Conception. More specifically, I will discuss circumstantial evidence to present the hypothesis that the wind stress curl near Point Conception contributes to the oceanic circulation in the western Santa Barbara Channel. This study statistically analyzes wind data from aircraft overflights in the spring of 1983, demonstrates a strong correlation between wind and wind stress curl, shows that atmospheric conditions in the spring of 1983 are similar to those in 1984, and, finally, interprets oceanic conditions in the spring of 1984 with the wind patterns of 1983 in mind. The wind stress curl near Point Conception will emerge as one of several potentially important forcing mechanisms for the circulation in the western Santa Barbara Channel.

2. Data sources and study area

Aircraft wind observations constitute the main data source of this study. In April and May of 1983 the NCAR aircraft *Queen Air* surveyed the wind field near Point Conception. Friehe et al. (1984) describe the instrumentation aboard the aircraft and its capability to measure winds over the coastal ocean off northern California. The appendix presents details of the wind calibration, the estimation of wind stresses, and the errors in derived quantities. Figure 1 shows the track of each of 20 airborne wind field surveys that took about 3–4 hours to complete. The sea breeze in the study area can reach amplitudes of 1–3 m s^{-1} (Brink et al. 1984; Caldwell et al. 1986), however, these winds diminish rapidly away from the coast. Nevertheless, some temporal aliasing is certainly present even though the synoptic winds are an order of magnitude larger than the sea breeze. Stuart and Linn (1983) describe the initial processing, which includes the interpolation of the data onto a regular grid with distances $\Delta x = 5.7$ km and $\Delta y = 3.7$ km where x and y represent longitude and latitude,

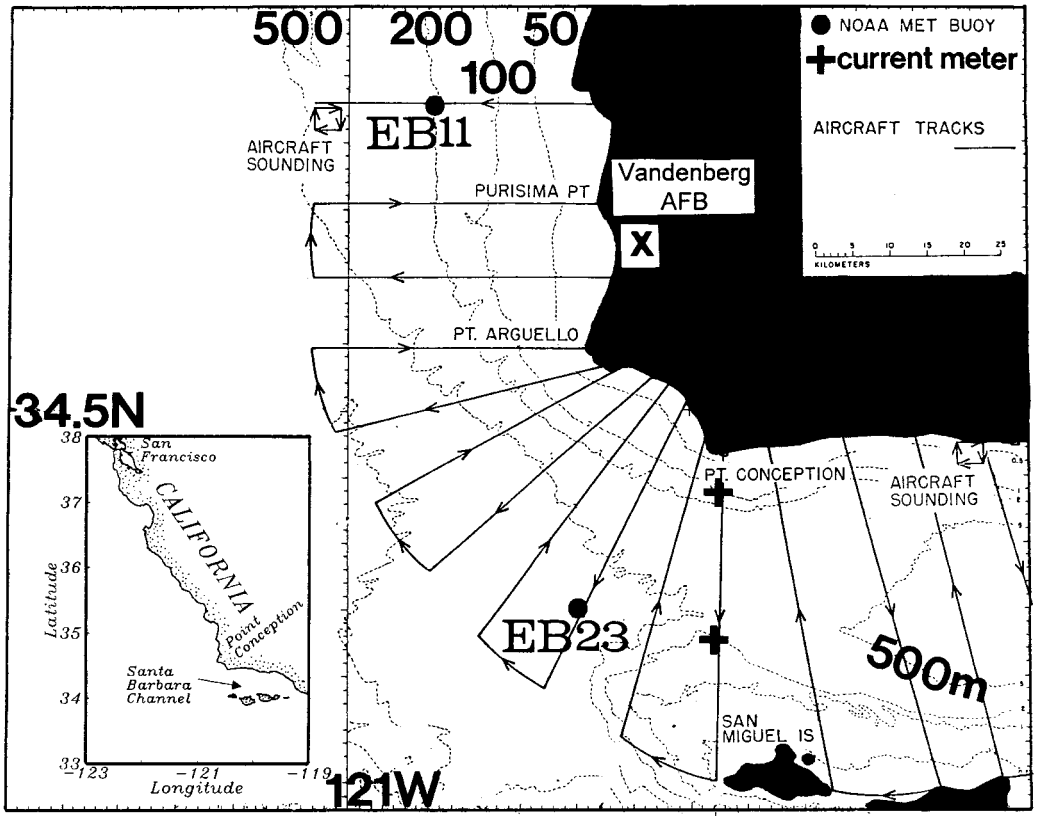

FIG. 1. Map of the study area. The insert shows the location of the Santa Barbara Channel whose western entrance at Point Conception is shown with aircraft flight tracks and bottom contours. Also shown are the locations of rawindsonde soundings at Vandenberg Air Force Base (AFB) and current meter moorings. Dashed contours represent bottom depths at 50, 100, 200, and 500 m. EB23 and EB11 refer to the NOAA environmental buoys 46023 and 46011, respectively. Note also the two locations of vertical aircraft soundings used to calibrate flight level wind measurements to surface wind stress estimates along with data from buoys EB11 and EB23.

respectively. The gridded wind stress field is a function of position (x_i, y_j) and time t_k; that is, $\boldsymbol{\tau} = \boldsymbol{\tau}(x_i, y_j, t_k)$ where i, j, k are integers from 1 to N, M, and K. A bold variable, such as $\boldsymbol{\tau}$, represents a vector while a nonbold variable denotes a scalar. An overbar indicates a temporal average; that is,

$$\overline{\tau}(x, y) = \frac{1}{K} \cdot \sum_{k=1}^{K} \tau(x, y, t_k) \tag{1}$$

and a vertical bar represents a spatial average; that is,

$$|\tau|(t) = \frac{1}{NM} \sum_{i=1}^{N} \sum_{j=1}^{M} \tau(x_i, y_j, t). \tag{2}$$

The spatially variable part of a field can then be written as $\tau_c(x, y, t) = \tau(x, y, t) - |\tau|(t)$. The spatial average of this property is by definition zero; that is, $|\boldsymbol{\tau}_c(x, y, t)| = 0$ while its spatial gradients are identical to those of the original field, for example,

$$\nabla \times \boldsymbol{\tau}_c(x, y, t) = \nabla \times \boldsymbol{\tau}(x, y, t). \tag{3}$$

Ekman pumping results from Ekman flux divergence and convergence, which in turn are caused by a spatially variable wind field. In order to conserve mass, a vertical velocity w results, which is (Gill 1982)

$$w = \mathbf{k} \cdot \left(\nabla \times \frac{\boldsymbol{\tau}}{f\rho} \right), \tag{4}$$

where f, ρ, $\boldsymbol{\tau}$, and $\mathbf{k}$ are Coriolis parameter, density of the water, wind stress, and vertical unit vector, respectively.

Current observations are available from instruments that in 1984 were moored inside the Santa Barbara Channel, which is approximately 150 km long, 10–30 km wide, and generally more than 200 m deep. A central basin is deeper than 600 m and two shelf regions are shallower than 200 m and narrower than 15 km. The present study uses current meter and CTD data from the 1984 experiment. Hydrography from 1983 is available, but it reflects conditions during weak and variable wind forcing only. Finally, wind and sea surface temperature data from NDBC meteorological buoy 46023 (shortened to EB23 in the following) complement the above data.

The present study synthesizes data from three observational experiments. Table 1 lists these and five more

TABLE 1. Experiments in the Point Conception area: DOE stands for Department of Energy, OPUS stands for Observations of Persistent Upwelling Systems, SBC stands for Santa Barbara Channel, and CCCCS stands for Central California Coastal Circulation Study. The data used in this study are indicated by an asterisk.

Year	Experiment	Instrumentation	Peer-reviewed reference	Figure in text
1964	DOE	Bottles, drifters	None	
1981	OPUS Pilot	CTD	Brink et al. (1984)	
		Aircraft winds	Brink et al. (1984)	
1983	OPUS	CTD	Atkinson et al. (1986)	
		XBT	Atkinson et al. (1986)	
		AVHRR	Atkinson et al. (1986)	
		ADCP	Barth and Brink (1987)	
		Drifter	Barth and Brink (1987)	
		Aircraft winds*	None	Figs. 3–9
		Current meters	Brink and Muench (1986)	
1983	SBC Pilot	Current meters	Brink and Muench (1986)	
		CTD	None	
1984	SBC	Current meters*	Auad et al. (1998), Münchow (1998)	Figs. 10–11, 12, 14
		CTD*	None+	Figs. 12–13, 14
		AVHRR	Lagerloef and Bernstein (1988)	
		Drifter	None	
1984–1985	CCCCS	Current meters*	Chelton et al. (1988)	Fig. 12
		CTD	None	
1989	EXXON	ADCP	None	
1992–1995	SBC	AVHRR	None	
		Current meters	Harms and Winant (1998)	
		Drifters	Dever et al. (1998)	
		ADCP	None	
		CTD	None	

+ Lagerloef and Bernstein (1988) use a map of SST from a CTD survey and record mean current vectors from moored current meters.

conducted near Point Conception. Peer reviewed papers refer to publications that describe the data in detail where they are available. All except the 1983 OPUS studies were motivated by offshore oil drilling operations. Most of the data listed in Table 1 are archived at the Scripps Institution of Oceanography where it can be accessed through the World Wide Web (http://www-ccs.ucsd.edu/zoo).

3. Spring 1983: Wind observations

Dorman and Winant (1995) statistically analyze the 10-yr record of meteorological buoys deployed in the coastal ocean off the western United States. They describe the wind field at large spatial (>200 km) and temporal (>1 month) scales. They find the strongest winds off Point Conception in the spring. In contrast, this study discusses the local wind field near Point Conception at much smaller spatial (<50 km) and temporal (<1 month) scales in the spring of 1983. The following five subsections introduce the atmospheric conditions with data from rawindsondes (section 3a), discuss three cases of the observed wind fields $\boldsymbol{\tau}(x, y, t_k)$ (section 3b), describe the properties of the temporally averaged field $\overline{\boldsymbol{\tau}}(x, y)$ (section 3c), study all fields $\boldsymbol{\tau}_c(x, y, t)$ with a complex EOF (CEOF) analysis (section 3d), and close with a correlation analysis of wind stress and wind stress curl (section 3e).

a. Atmospheric stratification

Figures 2a and 2b show the wind vector and the sea surface temperature at buoy EB23 (see Fig. 1 for location) as a low-pass filtered time series for the time period when the aircraft surveyed the wind field in the lower atmosphere. The (Lanczos) filter has a half-power point at 17 h and passes 90% and 10% of the variances at periods of 27 and 12 h, respectively. It thus removes most of the diurnal variability. Weak (<10 m s^{-1}) and variable winds occur during April and early May of 1983 (Fig. 2a) while strong (>10 m s^{-1}) and upwelling favorable winds persist after day 126 (6 May). The sea surface temperature then drops by 3°C within 3 days near day 130 (Fig. 2b). The observational period of the aircraft data thus covers both persistent upwelling and intermittent up- and downwelling-favorable winds. The hydrographic data are more limited to periods of weak and variable winds (Fig. 2b).

At Vandenberg Air Force Base (see Fig. 1 for location) vertical profiles of atmospheric properties are measured twice daily with a rawindsonde. The temperature and pressure data from these profiles allow estimation of the stability or buoyancy frequency N, which describes the vertical density stratification of the atmosphere for descending air (Gill 1982); that is,

$$N^2 = \frac{g}{T}\left(\frac{\partial T}{\partial z} + \Gamma\right), \tag{5}$$

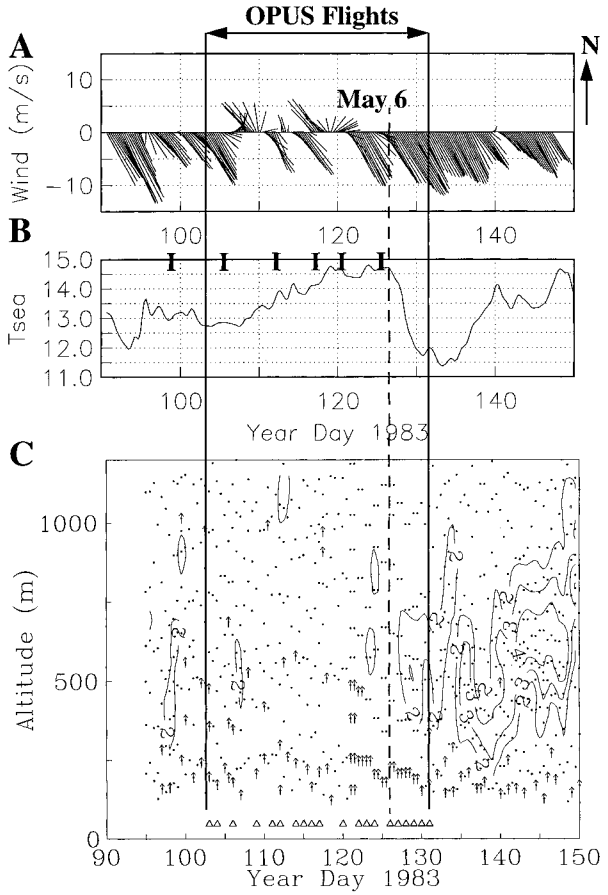

FIG. 2. Time series of (a) winds at EB23, (b) sea surface temperature (SST) at EB23, and (c) buoyancy frequency (N) in the lower atmosphere at Vandenberg AFB (Fig. 1).The units in (c) are 10^{-2} s^{-1} and, for clarity, only contours $>1 \times 10^{-2}$ s^{-1} are shown. Note the onset of persistent upwelling favorable winds near day 126 (6 May), which occurs concurrently with decreasing SST and increasing N in the atmosphere. The flow becomes supercritical ($F = U/(ND) > 1$) for wind speeds $U = 10$ m s^{-1}, vertical scale of motion $D = 500$ m, and buoyancy frequency $N > 2 \times 10^{-2}$ s^{-1}. Note also that all CTD surveys [vertical bars in (b)] were done prior to the persistent upwelling-favorable winds. The times of the 20 aircraft flights are indicated at the bottom of (c) as triangles. Dots indicate the location of measurements. Unstable vertical density gradients are indicated by a vertical arrow.

where $\Gamma = g/c_p$ is the dry adiabatic lapse rate, g is the gravitational constant, and c_p is the specific heat at a constant reference pressure. Figure 2c depicts the stability frequency N as a function of time and height. Until day 126 (6 May) N is less than 0.02 s^{-1}; that is, little vertical stratification exists and the moist adiabatic lapse rate $\Gamma_s < \Gamma$ should then be used to determine N. After day 126 a distinct stability maximum of about 0.04 s^{-1} develops on day 145 (24 May) about 500 m above the sea surface. Inspection of individual temperature and humidity profiles (not shown) reveals that the stability maximum represents a temperature inversion with warm dry air aloft and cool moist air below. The emerging vertical stratification in the lower atmosphere coincides with strongly upwelling-favorable winds. The coastal upwelling lowers the sea surface temperature, which enhances the vertical stability and reduces the frictional drag at the air–sea interface (Brown and Liu 1982). Some positive feedback between atmospheric stratification, oceanic upwelling, and upwelling-favorable winds thus may exist.

Following Winant et al. (1988), I define a local Froude number $F \equiv U/(ND)$, which constitutes a useful parameter to qualitatively describe the atmospheric flow. Here U and (ND) are the particle and the internal phase velocity, respectively; D represents the vertical scale of motion. The Froude number becomes larger than 1 after day 126 when typical scales are $U \sim 15$ m s^{-1} for the wind velocity (Fig. 2a), $D \sim 500$ m for the vertical scale of the motion, and $N \sim 0.04$ s^{-1} for the stability frequency. The flow is then supercritical and no internal waves can propagate against the flow. The energy of internal perturbations is then either trapped near the cape or swept downstream by the flow. The upstream conditions remain unchanged.

b. Case studies

The strongest upwelling favorable wind event lasting longer than 5 days occurred on day 128 (8 May, Fig. 3a). The spatial mean wind stress reached 0.31 Pa (Fig. 3b); the marine layer had a strong temperature inversion (not shown) and was about 500 m thick. The flow is supercritical (Fig. 2), separated from the coast, and Ekman pumping velocities reached 20 m day^{-1} off Point Conception (Fig. 3c). The spatial pattern of the large Ekman pumping extended into the western Santa Barbara Channel and was largely a result of the flow separation. Enriquez and Friehe (1995) find similar values for the wind stress curl near Point Arena off Northern California for both the 1982 CODE and 1989 SMILE data.

Four pulses of acceleration and deceleration (Fig. 3b) reveal a structure similar to that of an undular bore. These pulses do not, however, contribute strongly to the wind stress curl. They instead represent variations of the form $\partial_\theta v_\theta / r$ where v_θ and $r \cdot \theta$ are azimuthal velocity and distance in a radial geometry, respectively. A term $v_\theta \partial_\theta v_\theta / r$, however, indicates the nonlinearity of the atmospheric flow suggestive of hydraulic dynamics (Winant et al. 1988; Samelson 1992).

A less extreme case of large Ekman pumping is depicted in Fig. 4 for day 122 (2 May). The winds are moderately upwelling favorable (Fig. 4a) and the spatial mean wind stress is about 0.14 Pa (Fig. 4b). The spatial pattern of the Ekman pumping (Fig. 4c), however, closely resembles that of Fig. 3c. The flow separation is less abrupt than in the previous case, but the cyclonic circulation in the lee of the cape corresponds to a wind stress curl that causes up to 10 m day^{-1} Ekman pumping at the entrance of the Santa Barbara Channel.

Finally, Fig. 5 depicts the atmospheric flow in the

western part of the Santa Barbara Channel as a strong downwelling wind event passes the study area on day 109 (19 April) of 1983. The wind stress field appears trapped near the northern coast (Fig. 5a) where steep mountains rise to more than 1500-m height within 5 km of the coast. The atmosphere is continuously stratified during this event and no inversion is present. The laterally sheared flow, however, again corresponds to a cyclonic circulation to the southeast of Point Conception (Fig. 5b). Ekman pumping velocities at the entrance of the Santa Barbara Channel are thus again positive (Fig. 5c), that is, they indicate curl-induced upwelling by about 4 m day^{-1}. Downwelling of similar magnitude, however, occurs farther to the south. The horizontal scale of the atmospheric flow is about 10 km in the across-stream direction.

c. The ''mean'' wind field

Figure 6 shows the temporal mean field $\overline{\boldsymbol{\tau}}(x, y)$ that below is removed from each of the 20 maps. The mean wind stress during the observational period is from the northwest (Fig. 6a), that is, upwelling favorable, and generally exceeds 0.09 Pa. The area in the lee of Point Conception is the exception as there the flow separates from the coast. To the southeast of this ''shelter'' the flow accelerates. The acceleration and separation of the flow results in a cyclonic circulation, which becomes particularly clear in Fig. 6b. It depicts the same wind stress field as Fig. 6a, but the spatial mean $|\overline{\boldsymbol{\tau}}(x, y)|$ is subtracted from the data. The constant vector $|\overline{\boldsymbol{\tau}}(x, y)|$ in Fig. 6b represents a scale while the mapped vectors represent the spatially variable part of the wind field; that is,

$$\overline{\boldsymbol{\tau}}(x, y) = \overline{\boldsymbol{\tau}}(x, y, t) - |\overline{\boldsymbol{\tau}}(x, y)|. \quad (6)$$

Its dominant feature is the cyclonic circulation to the south of Point Conception.

The temporal mean wind stress causes about 4 m day^{-1} upwelling through Ekman pumping in an area 10 km wide and 80 km long (Fig. 6c). This area extends into the Santa Barbara Channel. Ekman pumping does not require a coastline and the vertical velocities are caused solely by the divergent Ekman fluxes of a spatially variable wind field. The coastal upwelling due to a wind stress adjacent to a coast is not included in Fig. 6c. There is no formal relationship between the upwelling caused by Ekman pumping and the upwelling caused by the coastal Ekman flux divergence. The latter depends upon the presence of the coast, takes place within an internal deformation radius of the coast (Gill 1982), and is not discussed. The Ekman pumping velocities reported here are of the same order of magnitude as modeled upwelling rates off the coasts of central California (Haidvogel et al. 1991).

d. The ''variable'' wind field

A complex empirical orthogonal function (CEOF) analysis systematically decomposes the spatial wind stress vector fields into a set of ordered statistical modes. Mathematically, these modes are the eigenvectors of the complex (Hermitian) covariance matrix of the observed vector field, which are written in the form $\boldsymbol{\tau}_c(x, y, t) = \tau_x + i \cdot \tau_y$ where the spatially variable vector $\boldsymbol{\tau}_c(x, y, t)$ is interpreted as a complex number and $i^2 = -1$. The zonal and meridional wind stress components τ_x and τ_y represent the real and imaginary part of $\boldsymbol{\tau}_c$, respectively. The eigenvalue λ to each eigenvector represents the amount of variance explained by this mode. Kundu and Allen (1976) and Kelly (1988) describe the method in detail. The decomposition of the observed field is a statistical, not a physical, decomposition. A common problem in any EOF analysis of temporally and spatially variable fields is to remove the correct means. I could remove either the spatial or the temporal, or both, means in either order. Kelly (1988) suggests removing both means when analyzing spatial variability. Hence the fields analyzed are $\boldsymbol{\tau}_c(x, y, t) = \boldsymbol{\tau}(x, y, t) - |\boldsymbol{\tau}(x, y, t) - \overline{\boldsymbol{\tau}}(x, y)|$.

Figures 7 and 8 depict the spatial pattern and temporal amplitudes of the largest three modes, respectively. The temporal amplitudes of Fig. 8 represent the (complex) amplification factors for the spatial patterns of Figs. 7a, 7c, and 7d. A unit vector pointing upward in Fig. 8 represents the pattern shown in Fig. 7 while a unit vector pointing sideways represents the same pattern rotated by 90 degrees. The temporal amplitudes are scaled such that the variance of the amplitude time series for each mode has uniform variance. Each modal pattern is also rotated such that the arrows in Fig. 7 point in the direction of the principal axis of the amplitude time series; that is, principal axes of the time series in Fig. 8 are vertical.

The first three CEOF modes here explain almost 90% of the variance (Fig. 7); however, only the first mode (72.5%) is statistically distinct since, as Fig. 7b indicates, the uncertainty of its eigenvalue $\delta\lambda = \lambda(2/N)^{1/2}$ does not overlap with that of any other eigenvalue (North et al. 1982). Here $N = 19$ is the degrees of freedom; the result does not change for $N = 6$. In contrast, the eigenvalues of mode 2 (10.8%) and mode 3 (6.4%) do overlap within their error bars and thus are not truly orthogonal of each other. Both are distinct from mode 4, however, and thus will be discussed as a coupled mode.

Mode 1 indicates a clear separation of the flow field near Point Conception. This separation is the main feature of the spatial wind field near Point Conception. The CEOF mode indicates a spatially coherent region of large and spatially variable horizontal Ekman fluxes and thus Ekman pumping. A ridge of minimum flow, but maximum curl, extends into the Santa Barbara Channel from a location at the coast between Point Arguello in

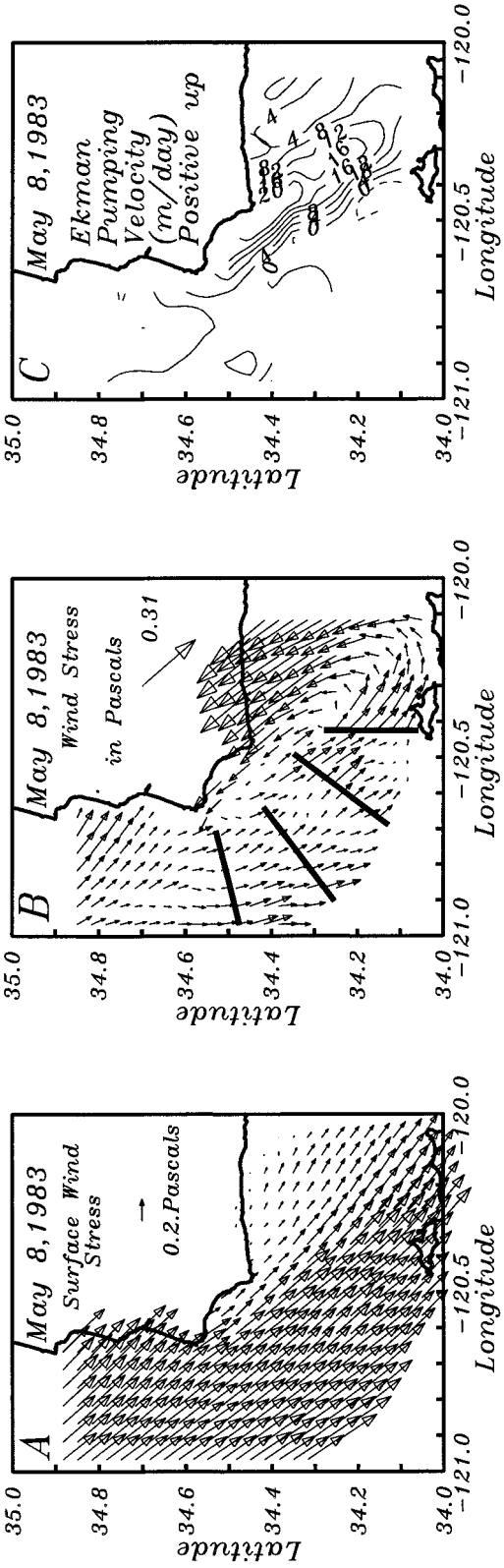

FIG. 3. Maps of (a) surface wind stress vectors, (b) deviations of the surface wind stress vectors from the spatial mean, and (c) vertical Ekman pumping velocities on day 128 (8 May 1983). The spatial-mean vector is displayed in the upper-right corner of (b) as a scale. Note the four pulses of acceleration as the flow turns, emphasized by the four solid lines. The Froude number for this event is larger than 1.5; i.e., the flow is supercritical (see Fig. 2).

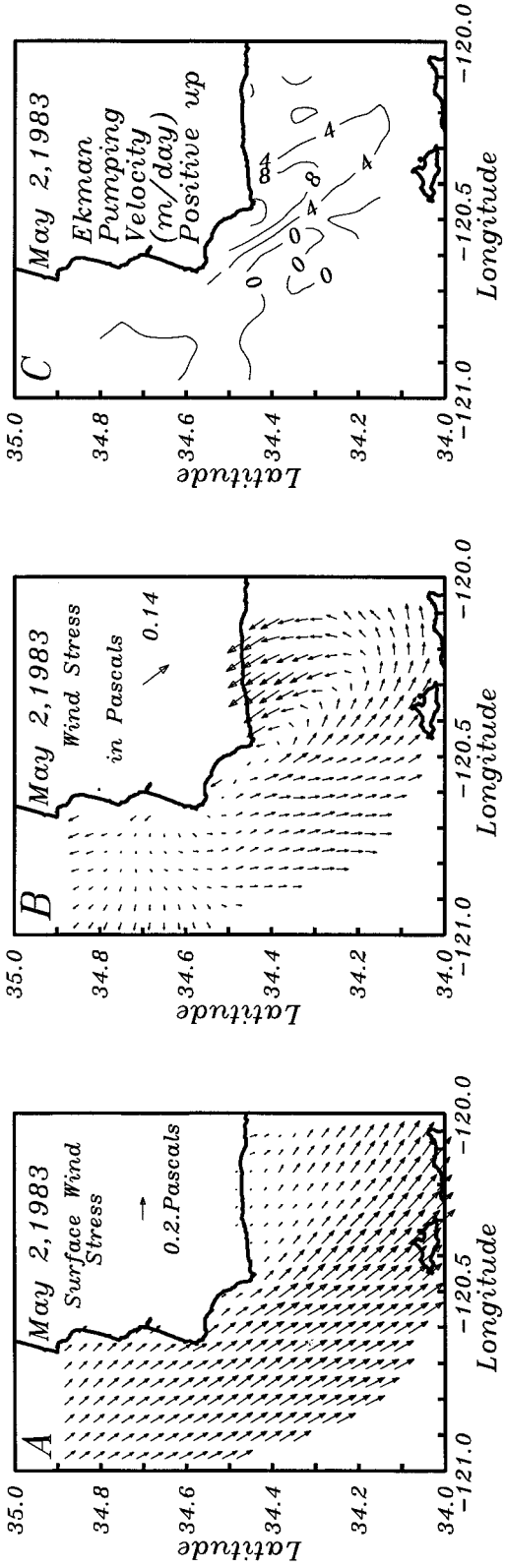

FIG. 4. As in Fig. 3 but for day 122 (2 May 1983).

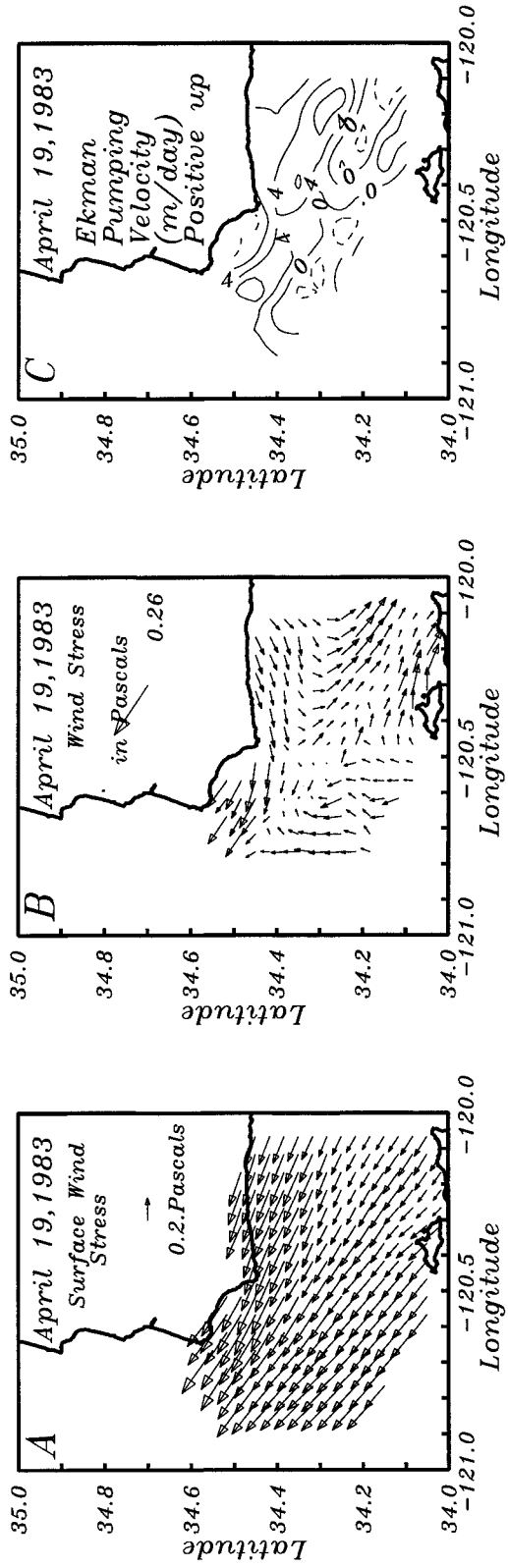

FIG. 5. As in Fig. 3 but for day 109 (19 Apr 1983).

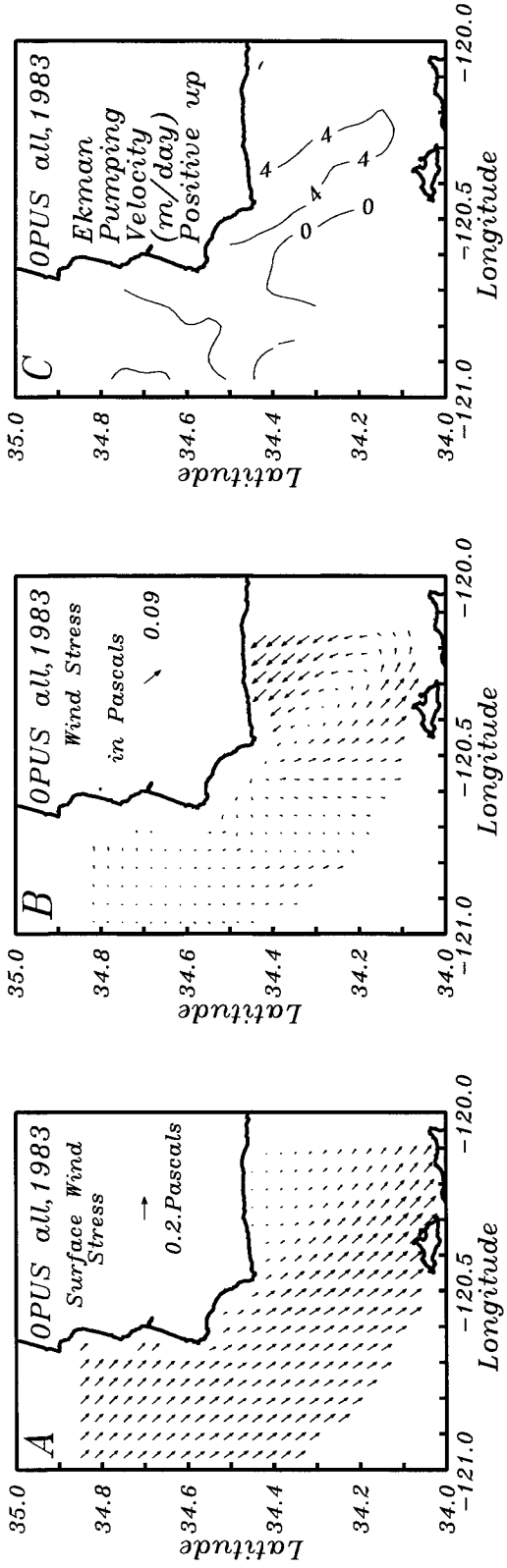

FIG. 6. As in Fig. 3 but for the temporal mean of all 20 maps.

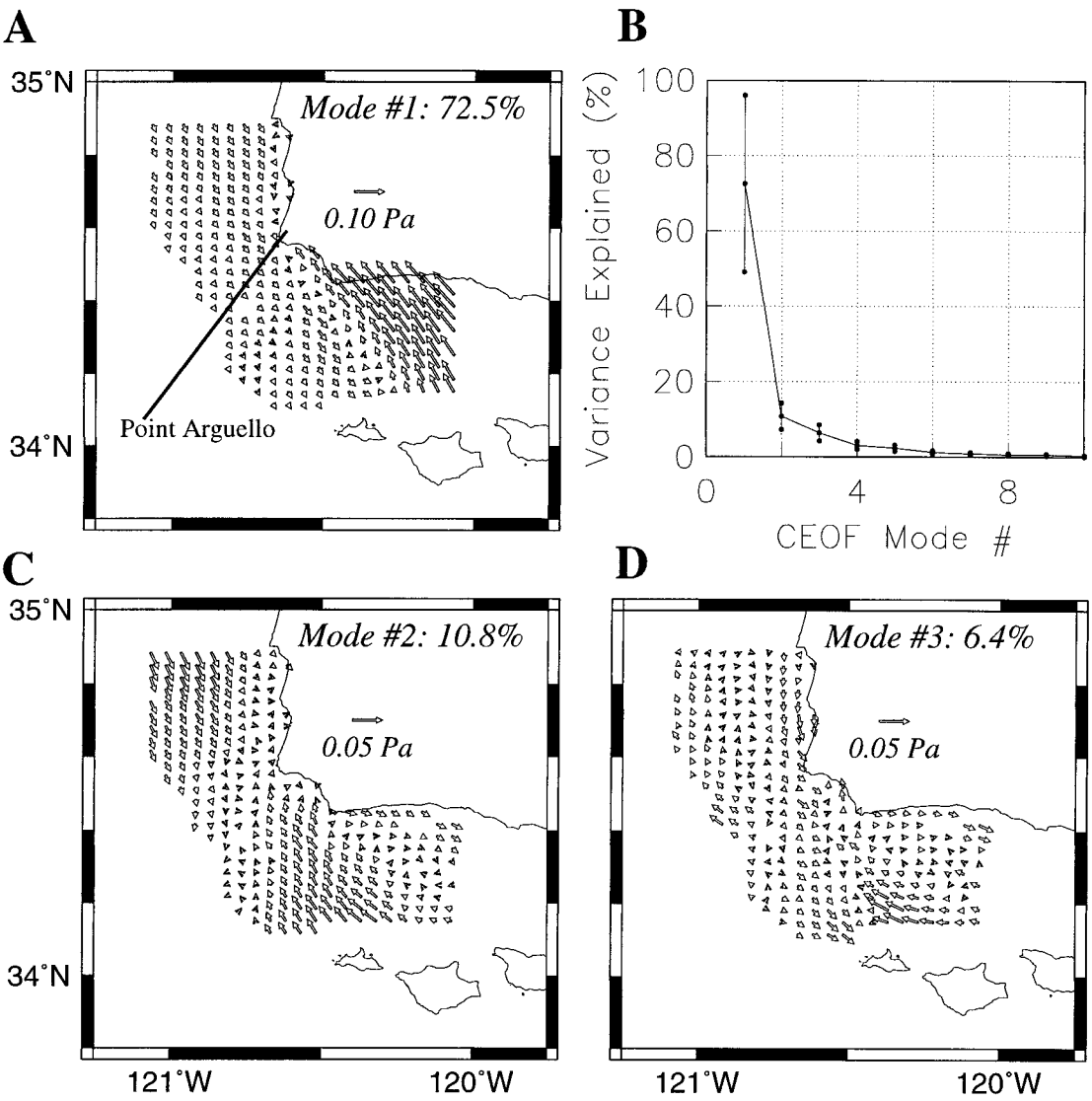

FIG. 7. Maps of the (a) first, (c) second, and (d) third CEOF modes of 19 windstress vector maps that account for 72.5%, 10.8%, and 6.4% of the total variance, respectively. (b) The variance explained along with estimates of their uncertainty for the first 10 (of 19) modes.

the north and Point Conception 20 km to the southeast (Fig. 7a). This ridge represents the inshore boundary of the flow as it separates from the coast. Closer inspection of Fig. 7a also reveals that the flow accelerates inshore near Point Arguello only to decelerate and accelerate again toward Point Conception. Much weaker wind stress curl of the opposite sign occurs farther offshore as winds and their gradients diminish in that direction.

Figure 8a shows the amplitudes of the wind stress anomalies, demonstrating that all except two maps contribute to the first mode. The two exceptions are the maps from day 104 (14 April) and day 126 (6 May) when the wind stress field is very close to its temporal mean state during the observational period. Mode 1 amplitudes (Fig. 8a) suggest two distinct temporal domains. From day 102 to day 125 the vectors are largely negative; that is, they indicate a downwelling tendency that weakens the mean state (Fig. 6). It reaches its minimum on day 117 (27 April 1983) when the wind field is downwelling favorable for a few days and the wind field is both strong and anticyclonic (not shown). After day 126 the amplitude vectors become positive; that is, they indicate an upwelling tendency that strengthens the cyclonic mean state. Toward the end of the record, when the lower atmosphere becomes vertically stratified (Fig. 2c), mode 1 thus represents a cyclonic wind stress curl during the strong upwelling-favorable wind events. The flow at this time is supercritical; low-level temperature inversions are present at 500-m height. This inversion is absent during the first 20 days of the record.

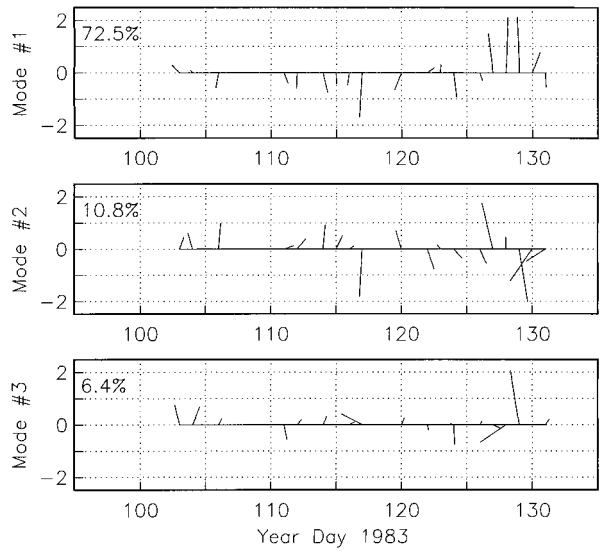

FIG. 8. Amplitudes of the first three temporal CEOF modes whose pattern is shown in Fig. 7. Units of the amplitude functions are arbitrary. The time series are scaled and rotated such that the total variance of each modal time series is 1 and its principal axis is vertical. The 19 vectors are connected with a solid base.

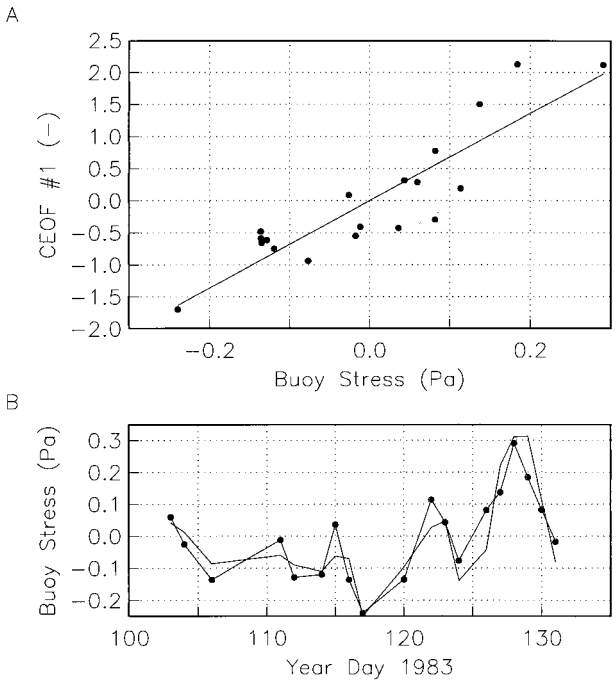

FIG. 9. Magnitude of the complex vector correlation between CEOF mode 1 amplitude and the wind stress at EB23. (a) The data scatter (symbols) and linear regression (line). (b) EB23 wind stress (line with symbols) and CEOF mode 1 (line only) as a function of time. The latter is scaled to fit the same scale as the buoy stress.

Modes 2 and 3 combine to explain an additional 17.2% of the variance. Together they describe weak convergent/divergent atmospheric flow. Such a spatial feature corresponds to a spatial acceleration/deceleration of the flow. In addition, these two modes appear to contain a weak shear region extending into the Santa Barbara Channel more aligned with the orientation of the channel as compared to the more oblique angle with which the ridge of large curl of mode 1 extends into the channel. The temporal amplitudes (Figs. 8b and 8c) are somewhat scattered and disorganized; that is, these two modes provide both smaller time and space scale variability that modifies the dominant flow described by mode 1.

In summary, mode 1 is strongest and cyclonic following day 126 (6 May 1983). It is at this time that the Ekman pumping would be largest as both the temporally mean (Fig. 6a) and variable (Fig. 7a) winds combine to result in the largest wind stress curl in the lee of Point Conception. The question arises if such enhanced upwelling over the center of the channel can be seen in hydrographic sections across the channel entrance in the form of doming isopycnals. The answer for the spring of 1983 is a ''no,'' for all such sections were taken during weak, intermittent, and even downwelling-favorable conditions (Fig. 2). Furthermore, the last 1983 OPUS section across the western entrance of the channel was taken on 5 May 1983 (day 125) a few days prior to the onset of the strong and persistent upwelling. The next question then arises: are doming isopycnals over the center of the channel seen in different years and, if so, is it possible to predict the wind stress curl from single point wind measurements? The answer to both these questions will be a ''yes.''

e. Wind stress curl prediction

The wind stress curl as represented by the first CEOF correlates strongly with the wind stress at EB23 (Fig. 9). Maximum vector correlation between the observed wind stress at buoy EB23 (Fig. 2a; see Fig. 1 for location) and the temporal amplitude of mode 1 (Fig. 8a) reveals $r_{12}^2 = 0.79$ that occurs at an angle of $-56°$; that is, wind stress correlates best with the pattern shown in Fig. 7a after it is rotated 56° clockwise from east. This orientation represents the direction of upwelling favorable alongshore winds. The correlation is significantly different from zero at the 95% confidence level for 18 ($r_{12}^2 > 0.2$) and 5 ($r_{12}^2 > 0.7$) degrees of freedom assuming wind stress decorrelation timescales of 2 and 6 days, respectively.

Figures 9a and 9b show the scatter and time series, respectively, of the vector components leading to this maximum correlation; in Fig. 9b the first CEOF mode $A_1(t)$ is scaled to fit the same graph as the wind stress. The wind stress at EB23 explains 79% of the variance of the first CEOF mode through the regression $A_1(t) = -0.9 + 6.8\tau$, where τ is the observed wind stress in Pa along 56° clockwise from east. The constant offset -0.9 represents the temporal mean wind stress (0.13

Pa) corresponding to the mean wind field (Fig. 6) that is excluded from the CEOF analysis. A measured wind stress at EB23 of 0.2 Pa thus adds to the mean curl the pattern, shown in Fig. 7a, scaled by 0.46 while a wind stress at EB23 of 0.3 Pa adds to the mean curl the pattern, shown in Fig. 7a, scaled by 1.14, thus roughly doubling the mean Ekman pumping shown in Fig. 6.

4. Discussion

In summary, winds generally separate from the coast near Point Conception and result in a cyclonic atmospheric circulation. This pattern emerges from daily maps of the wind stress (Figs. 3–5), from the roughly monthly average of 20 maps (Fig. 6), as well as from a CEOF analysis of wind stress anomalies (Fig. 7). The spatially variable winds and associated Ekman flux divergence correspond to up to 20 m day^{-1} upwelling, however, values of about 4–8 m day^{-1} are more typical. The largest curl-driven Ekman pumping occurs in an area to the southeast of Point Conception that extends about 30–50 km into the Santa Barbara Channel. The first CEOF mode correlates strongly with the winds observed at the meteorological buoy EB23 and a simple linear regression explains 57% ($72.5\% \times 0.79 = \lambda_1 r_{12}^2$) of the total variance of the spatial and temporal variability of the wind stress field in the spring of 1983. The wind stress curl near Point Conception is both a robust and a recurring feature. The next question is how does this robust wind stress curl affect the internal mass field at the entrance of the Santa Barbara Channel? Does it contribute to the oceanic circulation in the western approaches of this channel?

Harms and Winant (1998) identify six characteristic patterns from EOF analyses of a year-long 1994 current record of surface currents. All but one of these patterns show cyclonic current shear at the western entrance of the Santa Barbara Channel. The dynamics of the cyclonic circulation in its five different flavors, however, is still unknown. Harms and Winant (1998) and Dever et al. (1998) comment on pressure gradient and local wind forcing, while recent modeling work (Oey 1996; Wang 1997) adds that lateral friction and small-scale spatial variations in the wind field also contribute to the cyclonic circulation. The following discussion presents circumstantial evidence to justify the hypothesis that the flow in the Santa Barbara Channel is partly forced by the wind stress curl near Point Conception.

Figures 10a and 10b compare time series of wind observations from buoy EB23 for a 60-day period in the spring of 1983 and 1984, respectively. Markers in Figs. 10a and 10b indicate the time of CTD surveys. The 1983 CTD surveys sampled the oceanic density field during weak, variable, and often downwelling favorable wind conditions. Hence, no hydrographic observations are available for the period when the most intense upwelling and Ekman pumping takes place. In contrast, the 1983 aircraft surveys sampled all wind

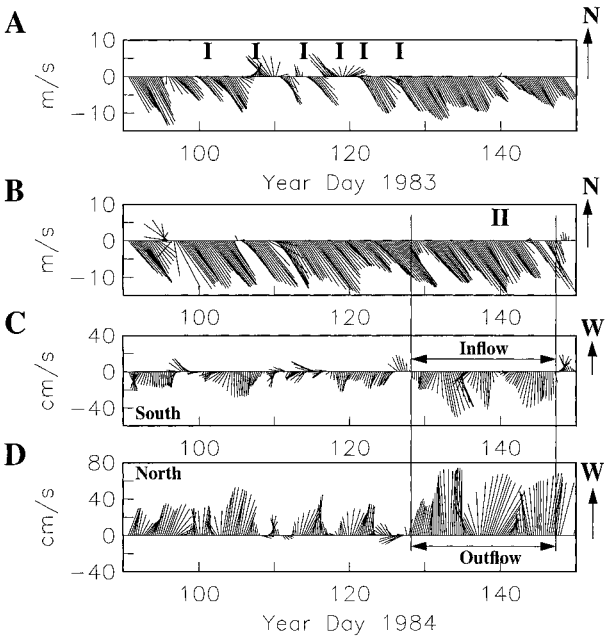

FIG. 10. Time series of (a) spring 1983 winds at EB23, (b) spring 1984 winds at EB23, (c) 30-m currents at the southern channel entrance, and (d) 30-m currents at the northern channel entrance. The symbols toward the top in panels (a) and (b) indicate the time hydrographic sections were collected across the western entrance of Santa Barbara Channel.

conditions including the strong and persistent upwelling following day 126 (Figs. 2, 3, and 9). It also contrasts with the conditions during a single CTD survey conducted in the spring of 1984, which, it appears in Fig. 10, sampled the density field during strong and persistently upwelling favorable winds.

Figures 10c and 10d show a 60-day segment of a 6-month long record of 30-m currents on the southern and northern shelf, respectively. From about day 128 through day 148 currents on the northern shelf $u(y_1)$ are out of the channel and reach 80 cm s^{-1} (Fig. 10d). In contrast, currents on the southern shelf $u(y_2)$ are into the channel and reach 40 cm s^{-1} (Fig. 10c). The winds at EB23 during this period of time (that includes a CTD survey on day 139, 19 May) are upwelling favorable and exceed 10 m s^{-1} for almost the entire 20-day long period. Note that offshore wind, currents, and lateral current shears fluctuate at a 5–10 day timescale. The response to the wind field is not always instantaneous and forcing mechanisms other than the local winds contribute to the flow field and its lateral shear.

Figure 11 shows the result of a frequency-domain cross-correlation analysis of the full 6-month record from January through July of 1984. It indicates significant coherence (variance explained) between the across-channel shear $\delta u = u(y_1) - u(y_2)$ and the wind stress. Two distinct spectral peaks emerge at periods of about 6 and 3.8 days that explain, respectively, 40% and 55% of the variance (Fig. 11). The correlated motion at

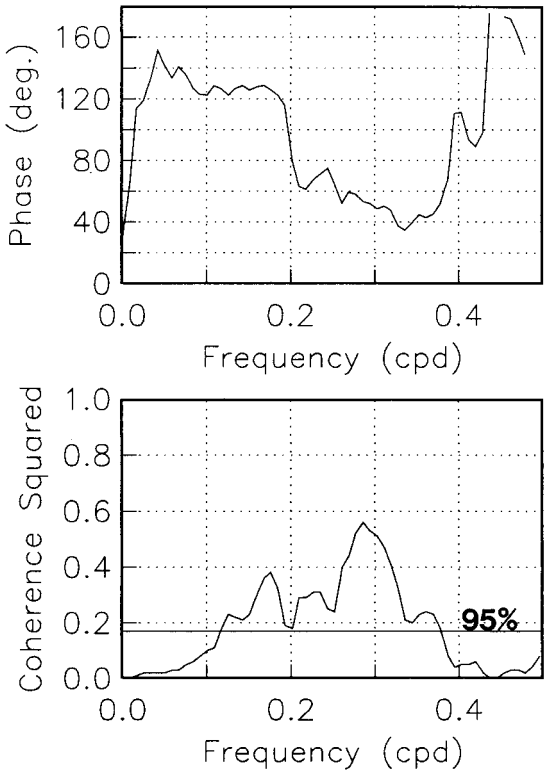

FIG. 11. Frequency domain correlation (coherence squared) between lateral current shear and alongshore windstress: (upper panel) the phase lag of the lateral shear with respect to wind stress and (lower panel) the fraction of the variance explained by a linear transfer function.

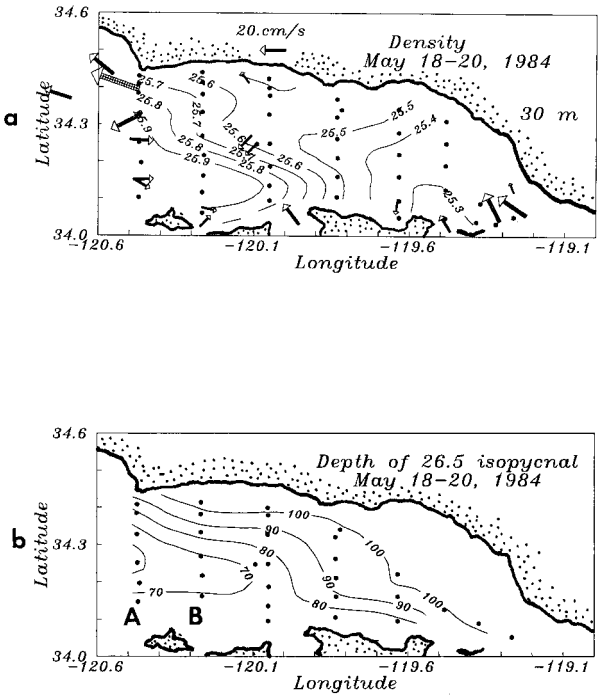

FIG. 12. Maps of the density and flow field of Santa Barbara Channel centered on day 140 (19 May 1984). (a) Horizontal distribution of density and currents at 30-m depth. Density data are from CTD casts while currents are from current meter moorings. (b) Depth of the 26.5 σ_t density surface. Labels ''A'' and ''B'' in (b) refer to the two density sections shown in Fig. 13. Filled circles indicate the location of CTD stations.

the short 3–4 day timescale lags the wind forcing by about 60° or 0.5 days. This short, almost instantaneous response is typical of a local, directly forced, wind-driven response. In contrast, the larger 120° phase lag at the longer 5–9 day timescale implicates a different forcing where the cyclonic shear lags the winds at EB23 by about 2–3 days. Auad et al. (1998) find similar correlations and phase lags in their more comprehensive analysis of all 1984 mooring data from the Santa Barbara Channel. While they comment on the poor correlation of surface currents with the winds, their EOF results for bandpassed data in a 4–6-day band indicates significant correlations with the wind. Their results and those presented here are consistent; that is, it is the cyclonic current shear [expressed in Auad et al. (1998) by the EOFs] not the surface currents that correlate with the winds at this frequency with a 2-day phase lag. Recall that the wind stress at EB23 correlates strongly with the wind stress curl near Point Conception (Fig. 9). It thus is conceivable that the wind stress curl results in the surface current shear at the 5–9 day timescale. A possible scenario on how the wind stress curl and Ekman pumping could set up such a circulation is presented next.

Figure 12a shows the density field at 30-m depth along with low-pass filtered current vectors at the same depth centered on the time of a 2-day CTD survey. The Lanczos filter has a half-power point at 84 h and passes 90% and 10% of the variance at 140 and 60 h, respectively. At the eastern entrance a 30 cm s^{-1} strong inflow transports lighter waters into the channel; however, lateral density gradients here are small. In contrast, strong lateral density gradients prevail in the western part of the channel where dense waters enter along the southern island chain, while buoyant waters leave the channel near Point Conception to the north (Fig. 12a). These buoyant waters occupy a surface layer about 40 m deep on the northern shelf/slope region only (Fig. 13).

A different picture emerges from density observations below the surface layer. Figure 12b shows how the depth of a particular density surface varies horizontally. The 26.5-σ_t surface is about 100-m deep along the northern shore. In most of the channel it slopes toward the surface from the northern shelf to the southern shelf where it is only about 80 m deep. South of Point Conception, however, the isopycnal is only 60 m deep and it is shallowest over the center of the channel. It deepens toward the southern shelf. This apparent doming of the density field becomes particularly clear in Fig. 13, which shows the density distribution of transects A and B across the western channel (see Fig. 12b for locations). All iso-

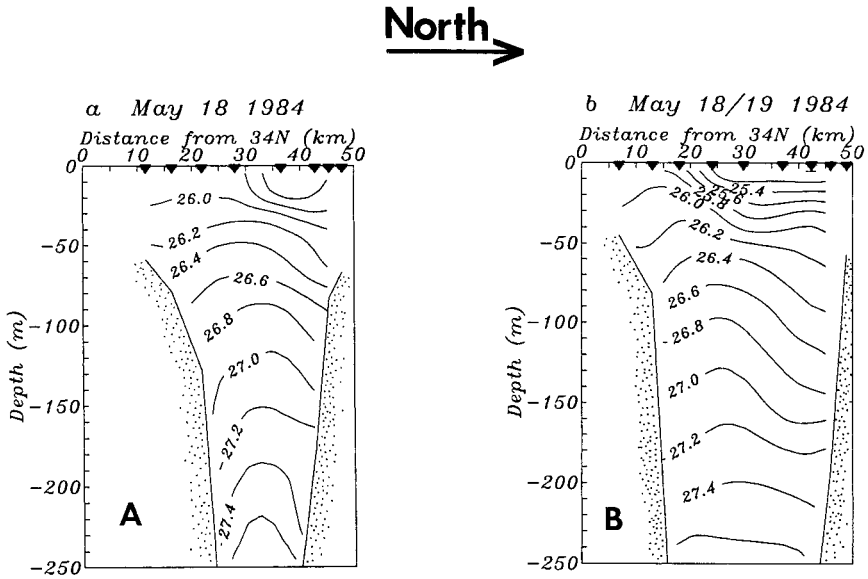

FIG. 13. Two density sections across the western Santa Barbara Channel. The locations for transects A and B, as shown in Fig. 12b, are labeled "A" and "B," respectively.

pycnals below 50 m are raised toward the surface at the center of the channel. Curl-driven upwelling would raise the isopycnal surfaces preferentially near the center of the channel (Fig. 6). If these doming isopycnals are furthermore geostrophically balanced, then they would indicate a cyclonic surface circulation relative to a stagnant deeper layer.

The thermal wind relation

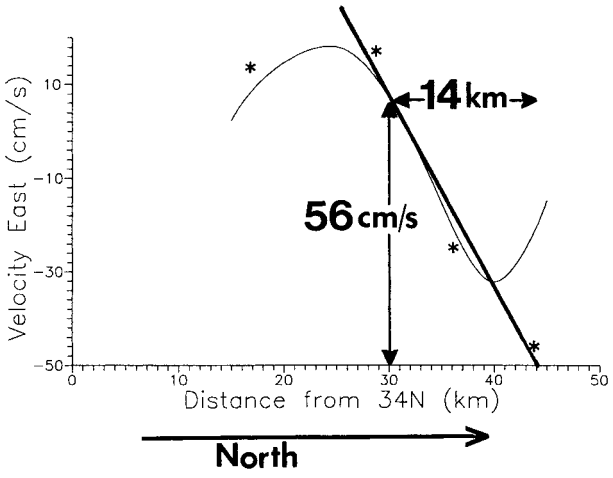

FIG. 14. Comparison of the alongchannel velocities at 30-m depth from current meter moorings (asterisks) with thermal wind velocities (thin line). The geostrophic thermal wind velocities at 30-m depth are the integral of the thermal wind shear from the bottom or the sill depth at 250 m (whatever is smaller) to 30-m depth. The thick solid line indicates a linear approximation of the across-channel velocity shear used in the main text to estimate the relative vorticity for the flow with $\Delta u = 56$ cm s^{-1} and $\Delta y = 14$ km, that is, $\Delta u/\Delta y = 0.56/14 \times 10^{-1}\ f = 0.36f$, where f is local Coriolis parameter (planetary vorticity).

$$\frac{\partial u}{\partial z} = \frac{g}{\rho_0 f}\frac{\partial \rho}{\partial y} \tag{7}$$

gives geostrophically balanced vertical current shears only. This shear is here arbitrarily referenced to zero flow at 250 m or, if the bottom is shallower than 250 m, to zero flow at the bottom. Figure 14 compares the geostrophic current profile across the channel at 30-m depth with observed low-pass filtered currents observed at the same depth during the CTD survey. The two curves generally agree to within 5 cm s^{-1} except at the northernmost mooring where the observed flow is about 20 cm s^{-1} stronger than the geostrophic flow. Hence, other mechanisms contribute to the flow here besides geostrophy if the reference level indeed represents a level of no motion. Nevertheless, the thermal wind relation reproduces the lateral current shear at 30 m rather well.

The relative vorticity ξ of the upper-layer fluid can be approximated by the lateral current shear; that is,

$$\xi = \frac{\partial v}{\partial x} - \frac{\partial u}{\partial y} \approx \frac{\partial u}{\partial y} \approx \frac{\Delta u}{\Delta y} = \frac{0.56}{14}\frac{\text{m s}^{-1}}{\text{km}} \approx 0.36f, \tag{8}$$

where the values for Δu and Δy are from Fig. 12 and $f = 1.1 \times 10^{-4}$ s^{-1}. The scale Δy closely corresponds to the internal deformation radius ND/f where $N^2 = (g/\rho)(\partial\rho/\partial z)$ is the square of the buoyancy frequency (about 6 cph) and D is the vertical scale of motion (about 50 m). These scales result in an internal deformation radius that is about 11 km. The ratio between the relative vorticity ξ and the planetary vorticity f corresponds to a Rossby number that measures the relative importance of nonlinear inertial to Coriolis forces (Münchow and Garvine 1993). Nonlinear inertial forces thus contribute

to the dynamics of the flow near Point Conception. It is conceivable that the advection of cyclonic vorticity (a nonlinear process) generated near Point Conception by the wind stress curl contributes to the dynamics of the western Santa Barbara Channel. Since the across-channel balance appears to be in geostrophic thermal wind balance, the nonlinear advective forces must contribute to the alongchannel balance. The dynamics at the western entrance of the channel thus appear to be semigeostrophic.

The link between the geostrophically balanced isopycnals and the wind stress curl is admittedly weak and circumstantial. The evidence appears sufficient, however, to justify the hypothesis that the wind stress curl at the western entrance of the Santa Barbara Channel affects the local circulation. The nonlinear advection of vorticity from this region into the channel is best investigated with surface drifter observations, such as described by Dever et al. (1998). In order to accurately predict the flow in the Santa Barbara Channel the wind stress curl thus must be included in numerical models of the channel circulation.

5. Conclusions

Near Point Conception the atmospheric flow separates from the mountainous coastline, which changes its orientation by about 90 degrees. A cyclonic circulation in the lower atmosphere emerges in the lee of the cape from both the temporal average of all wind data and from an analysis of the spatial variations from this average. More than 70% of the variance of the atmospheric flow is explained by a single statistical mode that describes cyclonic flow patterns during strong and persistent upwelling events. Supercritical flows exhibit a stronger than average cyclonic tendencies, but subcritical flows result in a cyclonic circulation as well.

The spatially variable atmospheric circulation corresponds to about 4–20 m day^{-1} vertical Ekman pumping velocities in the ocean. These inferred vertical velocities at the base of the surface Ekman layer could raise deep isopycnals and thus stretch vortex tubes in the ocean interior (Gill 1982). During strong upwelling events in the spring of 1984, isopycnals dome near the center of the Santa Barbara Channel where, in 1983, the core of the atmospheric cyclonic circulation was located. The persistent wind stress curl could thus have contributed to the doming of the isopycnals over the western center of the channel. In May 1984 moored current meters recorded a strong oceanic cyclonic circulation. During this event the thermal wind balance explains the across-channel structure of the alongchannel flow; however, the across-channel current shear suggests that the alongchannel momentum balance is not geostrophic. The dynamics is then semigeostrophic.

Near Point Conception many dynamically different regimes and processes overlap: eddies from the offshore California Current occasionally impinge upon the shelf (Atkinson et al. 1986); variable topography certainly scatters vorticity waves into smaller scale motions; and large temperature gradients between the two entrances of the Santa Barbara Channel force a buoyancy-driven circulation. All these processes interact with the wind-forced motions. It is hard observationally to separate these processes in order to understand the physics of their interaction. Idealized numerical models and laboratory studies, such as Wang (1997) and Klinger (1994), are needed in order to shed light on some of the physical processes that influence the flow near Point Conception and the western Santa Barbara Channel.

Acknowledgments. David Stuart of Florida State University generously provided computer print-outs of the gridded aircraft wind data. Nancy Bray supported me throughout the long duration of this study while Larry Atkinson, Myrl Hendershott, and Terry Paluszkiewicz provided encouragement at several critical junctures of this study. Early comments by Clinton Winant and the very thorough criticism of four reviewers improved the manuscript substantially over time. This study was begun with funds from the Mineral Management Service under Cooperative Agreement 14-35-0001-30571 to Scripps Institution of Oceanography. The final analyses, interpretations, and writing at Rutgers University were supported by the National Science Foundation through Grant OCE-95-28239.

APPENDIX

Calibration of Aircraft Winds

A careful calibration of the data is necessary in order to estimate the wind stress curl at the sea surface from aircraft measurements of winds aloft. During each survey the aircraft flew directly over meteorological buoys EB11 and EB23 (see Fig. 1 for locations). Figure A1 shows the scatterplot of 10-m buoy and 152-m aircraft winds along with linear regression curves for the east and north component of the wind vector. Table A1 summarizes the regression coefficients and their uncertainties at a 95% level to reject the null hypothesis. The correlation of buoy and aircraft winds is good; that is, more than 98% of the buoy variance is linearly related with the aircraft wind variance. The offset between the two measurements is zero with an uncertainty of 0.4 m s^{-1}. The speed of the buoy winds at 10 m is about 72% of the aircraft winds at 152 m to within an error of about 0.5%. The results of the regression are similar to those of Brink et al. (1984) off Point Conception; however, the errors on the regressions are smaller here because of the larger sampling size. Nevertheless, instrument and calibration uncertainties lead to errors in the wind speed of about 1 m s^{-1} with about 40% of the uncertainty arising from the maximum offset and 60% of the uncertainty arising from the uncertainty of the slope of the regression.

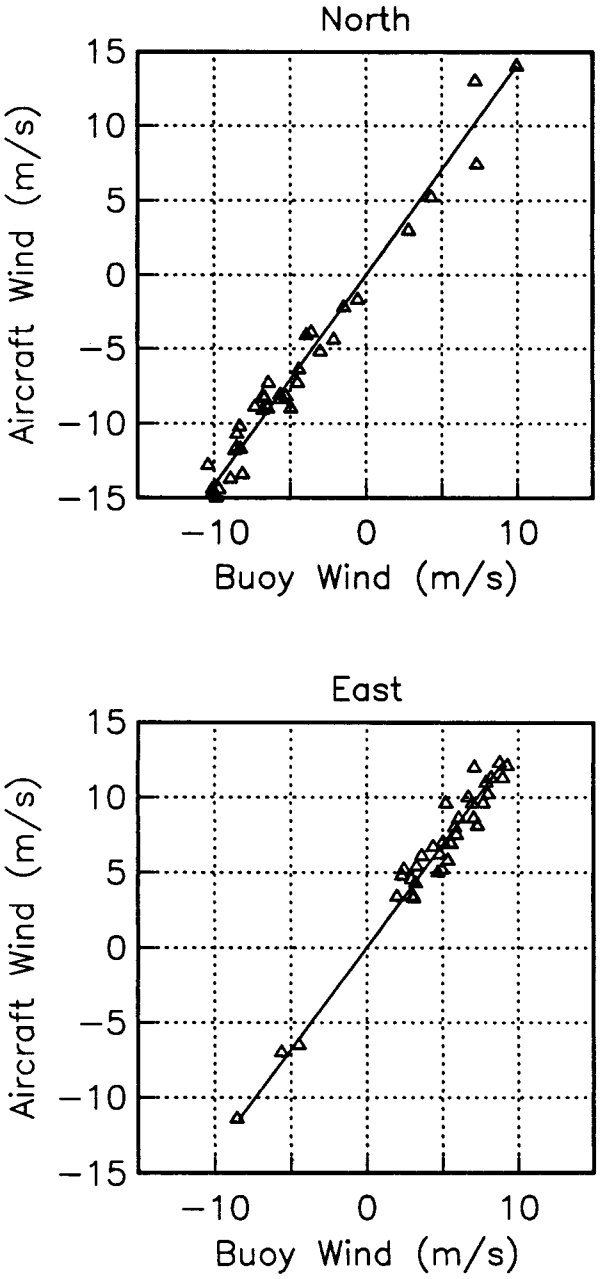

FIG. A1. Comparison of winds from the aircraft at 152 m with winds from meteorological buoys at 10 m. Linear regression lines are shown also (see Table A1).

The calibrated winds (Table A1) are converted to wind stress τ using the empirical bulk formulas of Wu (1980) $\boldsymbol{\tau} = (\rho_a/\rho_w C_{10}|\mathbf{U}_{10}|\mathbf{U}_{10}$ where ρ_a/ρ_w is the density ratio between air and water and C_{10} is an empirical drag coefficient for winds $\mathbf{U}_{10}$ measured 10 m above the sea surface. The drag coefficient is $C_{10} = (0.8 + 0.0656|\mathbf{U}_{10}|)10^{-3}$.

The wind stress curl, finally, is computed by central differences of the two components of the wind stress vector. It is thus estimated from the difference of four imperfectly estimated quantities. Furthermore, the measured-quantity wind must be cubed in order to obtain the estimated-quantity stress. Empirical tests reveal that this uncertainty in the wind speed causes an uncertainty in the Ekman pumping velocity of between 30% and 80%. These errors are upper limits and they depend upon the wind speed. Enriquez and Friehe (1995) find from a more comprehensive error analysis that their wind stress curl estimates are accurate within 0.13 Pa/100 km, which corresponds to an Ekman pumping velocity of about 1.2 m day^{-1}.

TABLE A1. Regressions between aircraft (152 m) and buoy (10 m) winds.

	Offset (m s^{-1})	Error offset (m s^{-1})	Slope	Error slope	r^2
East	−0.22	0.411	0.73	0.051	0.988
North	0.00	0.408	0.71	0.042	0.988

REFERENCES

Atkinson, L. P., K. H. Brink, R. E. Davis, B. H. Jones, T. Paluszkiewicz, and D. W. Stuart, 1986: Mesoscale hydrographic variability in the vicinity of Point Conception and Arguello during April–May 1983: The OPUS 1983 experiment. *J. Geophys. Res.*, **91,** 12 899–12 918.

Auad, G., M. C. Hendershott, and C. D. Winant, 1998: Wind-induced currents and bottom-trapped waves in the Santa Barbara Channel. *J. Phys. Oceanogr.*, **28,** 85–102.

Barth, J. A., and K. H. Brink, 1987: Shipboard acoustic Doppler velocity observations near Point Conception: Spring 1983. *J. Geophys. Res.*, **92,** 3925–3943.

Beardsley, R. C., C. E. Dorman, C. A. Friehe, L. K. Rosenfeld, and C. D. Winant, 1987: Local atmospheric forcing during the coastal ocean dynamics experiment. A description of the marine boundary layer and atmospheric conditions over a northern California upwelling region. *J. Geophys. Res.*, **92,** 1467–1488.

Bjerknes, V., 1901: Zirkulation relativ zu der Erde. Öfversikt af Kongl. Vet. Akad. Förhandl., No. 10, Stockholm, 739–775.

Brink, K. H., and R. D. Muench, 1986: Circulation in the Point Conception Santa Barbara Channel region. *J. Geophys. Res.*, **91,** 877–895.

——, D. W. Stuart, and J. C. Van Leer, 1984: Observations of the coastal upwelling region near 34°30′N off California: Spring 1981. *J. Phys. Oceanogr.*, **14,** 378–391.

Brown, R. A., and W. T. Liu, 1982: An operational large scale marine PBL model. *J. Appl. Meteor.*, **21,** 261–269.

Caldwell, P. C., D. W. Stuart, and K. H. Brink, 1986: Mesoscale wind variability near Point Conception, California, during spring 1983. *J. Climate Appl. Meteor.*, **25,** 1241–1254.

Chelton, D. B., A. W. Bratkovich, R. L. Bernstein, and P. M. Kosro, 1988: Poleward flow off central California during spring and summer of 1981 and 1984. *J. Geophys. Res.*, **93,** 10 604–10 620.

Dever, E. P., M. C. Hendershott, and C. D. Winant, 1998: Statistical aspects of surface drifter observations of circulation in the Santa Barbara Channel. *J. Geophys. Res.*, **103,** 24 781–24 797.

Dorman, C. E., 1987: Possible role of gravity currents in northern California's summer wind reversals. *J. Geophys. Res.*, **92,** 1497–1506.

——, and C. D. Winant, 1995: Buoy observations of the atmosphere along the west coast of the United States, 1981–1990. *J. Geophys. Res.*, **100,** 16 029–16 044.

Eddington, L. W., J. J. O'Brian, and D. W. Stuart, 1992: Numerical simulation of topographically forced mesoscale variability in a well-mixed marine layer. *Mon. Wea. Rev.*, **120,** 2881–2896.

Ekman, V. W., 1905: On the influence of the earth's rotation on ocean currents. *Ark. Mat. Astron. Fys.,* **2,** 1–53.

Enriquez, A. G., and C. A. Friehe, 1995: Effects of wind stress and wind stress curl variability on coastal upwelling. *J. Phys. Oceanogr.*, **25,** 1651–1671.

Friehe, C. A., R. C. Beardsley, C. D. Winant, and J. P. Dean, 1984: Intercomparison of aircraft and surface buoy meteorological data during CODE-1. *J. Atmos. Oceanic Technol.,* **1,** 79–86.

Gill, A. E., 1982: *Atmosphere–Ocean Dynamics*. Academic Press, 662 pp.

Haidvogel, D. B., A. Beckmann, and K. S. Hedström, 1991: Dynamical simulations of filament formation and evolution in the coastal transition zone. *J. Geophys. Res.,* **96,** 15 017–15 040.

Halliwell, G. R., Jr., and J. S. Allen, 1987: The large-scale wind field along the west coast of North America, 1981–82. *J. Geophys. Res.,* **92,** 1861–1884.

Harms, S., and C. D. Winant, 1998: Characteristic patterns of the circulation in the Santa Barbara Channel. *J. Geophys. Res.,* **103,** 3041–3065.

Hermann, A. J., B. M Hickey, C. F. Mass, and M. D. Albright, 1990: Orographically trapped coastal wind events in the Pacific Northwest and their oceanic response. *J. Geophys. Res.,* **95,** 13 169–13 193.

Kelly, K. A., 1988: Comment on ''Empirical orthogonal function analysis of Advanced Very High Resolution Radiometer surface temperature patterns in the Santa Barbara channel.'' *J. Geophys. Res.,* **93,** 15 753–15 754.

Klinger, B. A., 1994: Baroclinic eddy generation at a sharp corner in a rotating system. *J. Geophys. Res.,* **99,** 12 515–12 531.

Kundu, P. K., and J. S. Allen, 1976: Some three-dimensional characteristics of low frequency current fluctuations near the Oregon coast. *J. Phys. Oceanogr.,* **6,** 181–199.

Lagerloef, G. S. E., and R. L. Bernstein, 1988: Empirical orthogonal function analysis of Advanced Very High Resolution Radiometer surface temperature patterns in the Santa Barbara Channel. *J. Geophys. Res.,* **93,** 6863–6873.

Maas, C. F., and M. D. Albright, 1987: Coastal southerlies and alongshore surges of the west coast of North America: Evidence of mesoscale topographically trapped response to synoptic forcing. *Mon. Wea. Rev.,* **115,** 1707–1738.

Münchow, A., 1998: Tidal currents in a topographically complex channel. *Contin. Shelf Res.,* **18,** 561–584.

——, and R. W. Garvine, 1993: Dynamical properties of a buoyancy driven coastal current. *J. Geophys. Res.,* **98,** 20 063–20 077.

Nansen, F., 1902: Oceanography of the North Polar Basin. The Norwegian North Polar Expedition 1893–1896. Scientific Results Vol. III, No. 9, Kristiana.

North, G. R., T. L. Bell, R. F. Cahalan, and F. J. Moeng, 1982: Sampling errors in the estimation of empirical orthogonal functions. *Mon. Wea. Rev.,* **110,** 699–706.

Oey, L.-Y., 1996: Flow around a coastal bend: A model of the Santa Barbara Channel eddy. *J. Geophys. Res.,* **101,** 16 667–16 682.

Samelson, R. M., 1992: Supercritical marine boundary layer flow along a smoothly varying coastline. *J. Atmos. Sci.,* **49,** 1571–1584.

Strub, T. P., J. S. Allen, A. Huyer, and R. L. Smith, 1987: Large scale structure of the spring transition in the coastal ocean off western North America. *J. Geophys. Res.,* **92,** 1527–1544.

——, P. M. Kosro, and A. Huyer, 1991: The nature of the cold filaments in the California Current System. *J. Geophys. Res.,* **96,** 14 743–14 768.

Stuart, D. W., and M. A. Linn, 1983: Meteorological and aircraft data for OPUS 1981. Florida State University Ref. FSU-MET-OPUS-83-1, 57 pp. [Available from A. Münchow, The Graduate College of Marine Studies, University of Delaware, Robinson Hall, Newark, DE 19716-3501.]

Sverdrup, H. U., 1938: On the process of upwelling. *J. Mar. Res.,* **1,** 155–164.

Wang, D.-P., 1997: Effects of small-scale wind on coastal upwelling with application to Point Conception. *J. Geophys. Res.,* **102,** 15 555–15 566.

Winant, C. D., C. E. Dorman, C. A. Friehe, and R. C. Beardsley, 1988: The marine layer off Northern California: An example of supercritical channel flow. *J. Atmos. Sci.,* **45,** 3588–3605.

Wu, J., 1980: Wind-stress coefficients over sea surface near neutral condition—A revisit. *J. Phys. Oceanogr.,* **10,** 727–740.